



# Study of the CP property of the Higgs boson to electroweak boson coupling in the VBF $H \rightarrow \gamma\gamma$ channel with the ATLAS detector

The ATLAS Collaboration

A test of CP invariance in Higgs boson production via vector-boson fusion has been performed in the  $H \rightarrow \gamma\gamma$  channel using  $139 \text{ fb}^{-1}$  of proton–proton collision data at  $\sqrt{s} = 13 \text{ TeV}$  collected by the ATLAS detector at the LHC. The Optimal Observable method is used to probe the CP structure of interactions between the Higgs boson and electroweak gauge bosons, as described by an effective field theory. No sign of CP violation is observed in data. Constraints are set on the parameters describing the strength of the CP-odd component in the coupling between the Higgs boson and the electroweak gauge bosons in two effective field theory bases:  $\tilde{d}$  in the HISZ basis and  $c_{H\tilde{W}}$  in the Warsaw basis. The results presented are the most stringent constraints on CP violation in the coupling between Higgs and weak bosons. The constraints on  $\tilde{d}$  are further tightened through combination with results from the  $H \rightarrow \tau\tau$  channel.

The violation of the charge-conjugation and parity (CP) symmetry is one of the three Sakharov conditions [1] needed to explain the observed baryon asymmetry of the universe. The only established CP violation source is the complex phase in the quark mixing matrix [2], from which the derived magnitude of CP violation in the early universe is insufficient to explain the observed value of the baryon asymmetry [3–5]. The discovery of the Higgs boson by the ATLAS and the CMS experiments [6, 7] at the Large Hadron Collider (LHC) [8] opened a new direction to search for sources of CP violation: the interactions of the Higgs boson. The Standard Model (SM) Higgs boson ( $H$ ) is even under simultaneous charge-conjugation and parity inversion. Any deviation from a pure CP-even interaction of the Higgs boson with other SM particles could be a new source of CP violation and also a direct indication of physics beyond the SM (BSM). The CP structure of Higgs boson couplings to electroweak gauge bosons and fermions has been studied extensively by the ATLAS and the CMS experiments [9–18]. The results are consistent with the SM prediction, and no sign of CP violation has been found yet.

A CP-odd component in the Higgs boson coupling to electroweak bosons ( $HVV$ ,  $V = W/Z$ ) can be described by adding dimension-6 operators to the SM Lagrangian, using an effective field theory (EFT) approach. The total matrix element ( $\mathcal{M}$ ) can be written as

$$|\mathcal{M}|^2 = |\mathcal{M}_{\text{SM}}|^2 + 2 \cdot c_i \cdot \text{Re}(\mathcal{M}_{\text{SM}}^* \mathcal{M}_{\text{CP-odd}}) + c_i^2 \cdot |\mathcal{M}_{\text{CP-odd}}|^2. \quad (1)$$

The first term describes the SM contribution. The second term (interference term) is CP-odd, representing a new source of CP violation in Higgs boson couplings, and is parameterized by the Wilson coefficient  $c_i$ . The third term (quadratic term) describes a CP-even BSM contribution parameterized by  $c_i^2$ . The interference term only affects CP-odd observables and does not contribute to CP-even observables, e.g. the inclusive cross-section [19].

Several methods were developed to construct CP-odd observables that can distinguish CP violation contributions, e.g. in Refs. [12, 17]. This study adopts the Optimal Observable [20–24] defined as  $OO = 2 \cdot \text{Re}(\mathcal{M}_{\text{SM}}^* \cdot \mathcal{M}_{\text{CP-odd}}) / |\mathcal{M}_{\text{SM}}|^2$  to test the CP structure of the Higgs boson coupling to electroweak bosons in vector-boson-fusion (VBF) production. This method combines event-based information from a multidimensional phase space into a single CP-sensitive observable. In the SM, the  $OO$  distribution is expected to be symmetric with a mean value of zero, and any asymmetrical effects would indicate contributions from the CP violation term, in the absence of rescattering by new light particles in loops [25]. For a given event, the matrix elements in the  $OO$  definition are calculated using the four-momenta of the Higgs boson and the two forward VBF jets, and have no dependence on the decay mode of the Higgs boson. This method was first introduced in the  $H \rightarrow \tau\tau$  analysis [9] by ATLAS and can be used in all Higgs boson decay channels.

This Letter reports an analysis to test the CP invariance of the  $HVV$  coupling by using the Optimal Observable method in the VBF  $H \rightarrow \gamma\gamma$  channel, using the  $139 \text{ fb}^{-1}$  of proton–proton ( $pp$ ) collision data at  $\sqrt{s} = 13 \text{ TeV}$  recorded during 2015–2018 with the ATLAS detector. The VBF signal yield in  $OO$  bins is extracted from a simultaneous fit to the diphoton invariant mass spectra split into the  $OO$  bins, which is then used to determine the CP violation contributions to the  $HVV$  coupling.

Results are interpreted in two EFT bases: the HISZ [26] and Warsaw [27–29] bases. The HISZ basis is used in order to combine the results with the previous measurement from the  $H \rightarrow \tau\tau$  channel [9], whereas the Warsaw basis is used to provide measurements for future combinations with other Higgs boson measurements. In both bases, three Wilson coefficients multiplying CP-odd operators describe possible CP-odd couplings between the Higgs boson and electroweak gauge bosons. In the HISZ basis,  $\tilde{d}$  is

constrained by assuming  $\tilde{d} = \tilde{d}_B$  and setting the third coefficient to zero, as in Ref. [9]. In the Warsaw basis,  $c_{H\tilde{W}}$  is constrained by setting  $c_{H\tilde{B}}$  and  $c_{H\tilde{W}B}$  to zero. In both bases, all CP-even operators coefficients are set to zero. Constraints on all three coefficients in the Warsaw basis were obtained previously in the  $H \rightarrow ZZ$  channel [13, 16] and  $H \rightarrow \gamma\gamma$  channel using differential cross-sections [12]. The measurements have significant correlations since these channels cannot distinguish between the three operators. The VBF topology in this analysis is mainly sensitive to  $c_{H\tilde{W}}$  and could help to reduce this correlation.

The ATLAS detector [30–32] is a multipurpose particle detector with a forward-backward symmetric cylindrical geometry and near  $4\pi$  coverage in solid angle.<sup>1</sup> The trigger system consists of a hardware-based first-level trigger and a software-based high-level trigger [33]. Events used in this analysis were accepted by a diphoton trigger requiring the leading and subleading photons to have transverse energies ( $E_T$ ) greater than 35 GeV and 25 GeV, respectively, during the whole data-taking period. This trigger had a *Loose* photon identification requirement in 2015–2016 [34], but due to the increasing instantaneous luminosity the identification requirement was tightened for data-taking in 2017–2018 [34]. In addition, a single-photon trigger with *Loose* identification criteria and an  $E_T$  threshold of 120 (140) GeV in 2015–2016 (2017–2018) was used to recover events with collimated diphoton pairs with very high transverse momentum ( $p_T$ ) [34]. The average trigger efficiency is over 98% for events passing the full diphoton event selection for this analysis [34]. An extensive software suite [35] is used in the reconstruction and analysis of real and simulated data, in detector operations, and in the trigger and data acquisition systems of the experiment.

Higgs boson production via VBF was simulated with POWHEG BOX v2 [36] using the PDF4LHC15NLO [37] parton distribution function (PDF) set. The generation is accurate to next-to-leading-order (NLO) in QCD, and the total cross-section is normalized to a calculation including QCD corrections at full NLO and approximate next-to-next-to-leading-order (NNLO) accuracy as well as electroweak (EW) corrections at full NLO accuracy [38–40]. Higgs boson production via gluon-gluon fusion (ggF) was modeled at NNLO accuracy in QCD using POWHEG BOX v2 [41, 42] and the NNLO family of PDF4LHC15 PDFs. The simulation achieves NNLO accuracy for arbitrary inclusive  $gg \rightarrow H$  observables by reweighting the Higgs boson rapidity spectrum in HJ-MiNLO [43–45] to that in HNNLO [46], and the total cross-section is normalized to a prediction calculated at next-to-next-to-next-to-leading-order (N<sup>3</sup>LO) accuracy in QCD and including NLO EW corrections [47–57]. Other Higgs boson production processes, e.g. in association with a vector boson ( $VH$ ) or top quark(s) ( $ttH$ ,  $tH$ ), were also modeled using POWHEG BOX v2. Prompt diphoton production ( $\gamma\gamma$ ) was simulated with the SHERPA 2.2.4 [58] generator. More details can be found in Ref. [12].

To simulate the effects of nonzero values of  $\tilde{d}$  and  $c_{H\tilde{W}}$  in the  $HVV$  vertex, a reweighting method is implemented for the HISZ basis and Warsaw basis, respectively, and applied to the aforementioned SM VBF signal sample. For the  $\tilde{d}$  coefficient in the HISZ basis, as detailed in Ref. [9], two weights are calculated by the HAWK program [38, 39, 59] for each event using generator-level information:  $w_1 = 2 \cdot \text{Re}(\mathcal{M}_{\text{SM}}^* \cdot \mathcal{M}_{\text{CP-odd}}) / |\mathcal{M}_{\text{SM}}|^2$  and  $w_2 = |\mathcal{M}_{\text{CP-odd}}|^2 / |\mathcal{M}_{\text{SM}}|^2$  with a specific amount of CP mixing (given in terms of  $\tilde{d}$ ), to model the contribution from the interference term and the quadratic term, respectively, as shown in Eq. (1). For the interpretation in the Warsaw basis, a reweighting of the

<sup>1</sup> ATLAS uses a right-handed coordinate system with its origin at the nominal interaction point (IP) in the center of the detector and the  $z$ -axis along the beam pipe. The  $x$ -axis points from the IP to the center of the LHC ring, and the  $y$ -axis points upwards. Cylindrical coordinates ( $r$ ,  $\phi$ ) are used in the transverse plane,  $\phi$  being the azimuthal angle around the  $z$ -axis. The pseudorapidity is defined in terms of the polar angle  $\theta$  as  $\eta = -\ln \tan(\theta/2)$ . Angular distance is measured in units of  $\Delta R \equiv \sqrt{(\Delta\eta)^2 + (\Delta\phi)^2}$ .

reconstructed  $OO$  distribution at different values of  $c_{H\bar{W}}$  is obtained by

$$\frac{d\sigma}{dOO} = \left(\frac{d\sigma}{dOO}\right)^{\text{NLO}} \cdot \left(\frac{d\sigma}{dOO}\right)_{c_{H\bar{W}}}^{\text{MG5}} / \left(\frac{d\sigma}{dOO}\right)_{c_{H\bar{W}}=0}^{\text{MG5}},$$

where ‘MG5’ labels the prediction from MADGRAPH [60, 61] using SMEFTSim [27, 28], and ‘NLO’ labels the aforementioned SM VBF signal sample. MADGRAPH events for nonzero values of  $c_{H\bar{W}}$  were generated setting the scale of new physics  $\Lambda = 1$  TeV and fixing all other Wilson coefficients to zero. For both interpretations, higher-order QCD and electroweak corrections are assumed to factorize from the new-physics effects. Limits in the two bases are extracted from the effect of the interference-only term and also from the effect of the interference-plus-quadratic terms. The  $OO$  value is calculated using HAWK because the  $HWW$  operators in the two EFT bases are similar. HAWK uses the HISZ basis assuming  $\tilde{d} = \tilde{d}_B$ , which corresponds to  $c_{H\bar{W}} = c_{H\bar{B}}$  for the Warsaw basis. However, since  $c_{H\bar{B}}$  has negligible impact on VBF, only  $c_{H\bar{W}}$  is varied (setting  $c_{H\bar{B}} = 0$ ) and the computed  $OO$  is assumed to be equally optimal for  $c_{H\bar{W}}$  only.

All generated events were passed through a full simulation of the ATLAS detector response [62] using GEANT4 [63], except the SHERPA  $\gamma\gamma$  sample, which was passed through a fast parametric simulation of the detector response [62]. The effects of multiple  $pp$  interactions in the same or neighboring bunch crossings (pileup) are included by overlaying events generated with PYTHIA 8 [64]. Events are weighted such that the distribution of the average number of interactions per bunch crossing matches that observed in data.

Photons are reconstructed from variable-size topological clusters formed from electromagnetic calorimeter cells with significant energy deposits and from tracks, initiated by converted photons, measured in the inner detector (ID) [65]. Events must have at least two photon candidates outside the calorimeter’s barrel/endcap transition region,  $1.37 < |\eta| < 1.52$ , and within  $|\eta| < 2.37$ , where the two leading (highest- $E_T$ ) photons are used to reconstruct the Higgs boson candidate and the primary vertex of the event [66]. The diphoton invariant mass  $m_{\gamma\gamma}$  is required to be in the range 105–160 GeV. The leading and subleading photons are further required to have  $E_T/m_{\gamma\gamma}$  greater than 0.35 and 0.25, respectively, and fulfill the *Tight* identification selection and *Tight* calorimetric and track-based isolation requirement [65]. Jets are reconstructed using the anti- $k_t$  algorithm [67, 68] with a radius parameter  $R = 0.4$  from inputs formed with a particle-flow algorithm [69], which uses information from both the calorimeter and the ID. Jet candidates are required to have  $p_T > 30$  GeV and  $|\eta| < 4.4$ . To suppress jets from pileup collisions, jet candidates with  $|\eta| < 2.4$  and  $p_T < 60$  GeV are required to pass the *Tight* jet vertex tagger (JVT) selection [70]. For jets with  $|\eta| \geq 2.4$ , the *Loose* forward JVT selection [71] is applied to remove pileup jet contamination. To construct the region enriched with VBF signal events, two loose criteria are applied: events must have at least two jets with pseudorapidity separation  $|\Delta\eta_{jj}| > 2$  and Zeppenfeld variable [72]  $\eta^{\text{Zep}} = |\eta_{\gamma\gamma} - (\eta_{j1} + \eta_{j2})/2| < 5$ .

To increase the VBF signal purity, two boosted decision trees (BDT) [73] are trained.  $\text{BDT}_{\text{VBF/ggF}}$  is used to separate VBF signal from ggF events, which are the major background from Higgs boson production.  $\text{BDT}_{\text{VBF/Continuum}}$  is used to distinguish VBF  $H \rightarrow \gamma\gamma$  events from continuum background events, which consist of the prompt diphoton events ( $\gamma\gamma$ ) and events where one or two of the photon candidates originate from jets misidentified as photons ( $\gamma j$  or  $jj$ ). The  $\gamma\gamma$  events, which are the dominant component of the continuum background, are obtained from simulation, while  $\gamma j$  and  $jj$  events are obtained from dedicated data control regions, as described later. The two BDTs use the same input variables: invariant mass of the dijet system formed by the two leading jets ( $m_{jj}$ ), pseudorapidity separation of the dijet system ( $\Delta\eta_{jj}$ ), perpendicular projection of the diphoton  $p_T$  onto the diphoton thrust axis ( $p_{\text{T}}^{\gamma\gamma}$ ) [74],  $p_T$  of the Higgs boson and the leading two jets ( $p_{\text{T}}^{Hjj}$ ), azimuthal angle between the diphoton and dijet systems

( $\Delta\phi(\gamma\gamma, jj)$ ), minimum angular separation between the photons and the two leading jets ( $\Delta R_{\gamma j}^{\min}$ ), and  $\eta^{Z_{\text{EPP}}}$ . These input variables are designed to be insensitive to the CP property of the VBF signal and to have negligible correlation with  $m_{\gamma\gamma}$ . Figure 1 shows the BDT output distributions of the VBF signal, the ggF background, the continuum background, and the data in the  $m_{\gamma\gamma}$  sideband ( $m_{\gamma\gamma} \in [105, 118]$  GeV or  $[132, 160]$  GeV). The comparison between the continuum background and the sideband data shows the continuum background used in the BDT training is well modeled. Events are categorized as follows: firstly, a requirement is placed on  $\text{BDT}_{\text{VBF/ggF}}$  to separate events into ‘tight’ (T) and ‘loose’ (L) regions. The ratio of VBF signal to ggF background is improved by a factor of ten in the ‘tight’ region. Then, two independent requirements on  $\text{BDT}_{\text{VBF/Continuum}}$  are applied to the ‘tight’ and ‘loose’ regions to maximize the combined significance of the VBF signal. Three signal regions are defined: TT, TL, and LT, where the first (second) letter corresponds to the  $\text{BDT}_{\text{VBF/ggF}}$  ( $\text{BDT}_{\text{VBF/Continuum}}$ ) separation type. More details on the BDT requirements can be found in the Appendix. In the TT and TL categories, the dominant Higgs boson backgrounds are from the ggF process, and the contributions from non-ggF Higgs processes, e.g.  $VH$ ,  $ttH$  and  $tH$ , are found to be negligible. In the LT category, Higgs boson backgrounds are still mostly from the ggF process, while those from non-ggF Higgs processes increase to about 1%–3% of the VBF event yield.

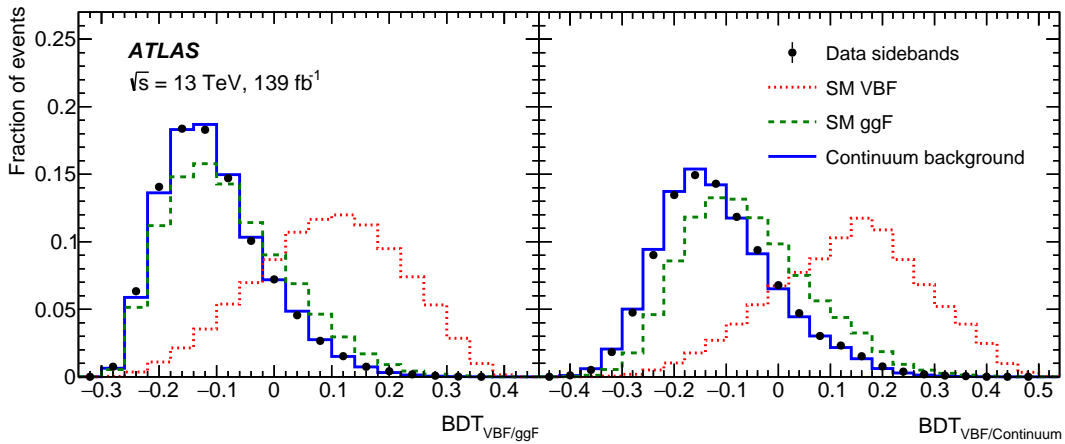


Figure 1: Distribution of the output of  $\text{BDT}_{\text{VBF/ggF}}$  (left) and  $\text{BDT}_{\text{VBF/continuum}}$  (right). The comparison between the continuum background and the sideband data indicates the continuum background used in the BDT training is well modeled.

The  $OO$  value is computed from the reconstructed four-momenta of the Higgs boson and the two VBF jets, from which the momentum fractions of the two initial-state partons are derived in the beam directions by exploiting energy-momentum conservation, as detailed in Ref. [9]. The signal yield is extracted via a combined unbinned maximum-likelihood estimation applied to the  $m_{\gamma\gamma}$  distribution of observed data in each  $OO$  bin, as shown in Figure 2. Both the signal and background shapes are modeled with analytic functions. The  $H \rightarrow \gamma\gamma$  signal shape is described by a double-sided Crystal Ball (DSCB) function [12], consisting of a Gaussian distribution in the region around the peak, continued by power-law tails at lower and higher  $m_{\gamma\gamma}$  values. The parameters of the DSCB function in each category are obtained by a fit to the simulated VBF sample, as well as other Higgs boson production modes in proportion to their SM cross-sections.

The modeling of the continuum background relies on both simulation and data-driven methods. The  $m_{\gamma\gamma}$  shape of the  $\gamma\gamma$  component is estimated using the SHERPA sample, while the  $m_{\gamma\gamma}$  shapes of the  $\gamma j$  and  $jj$

components are obtained using data control regions formed by inverting the *Tight* photon identification and isolation requirements. The template is then built by summing the  $\gamma\gamma$ ,  $\gamma j$  and  $jj$  components, where their fractions are measured in data using a two-dimensional double-sideband method [75]. The composition of the continuum background is found to be approximately 85%  $\gamma\gamma$  events and 15%  $\gamma j + jj$  events. The background templates are smoothed using Gaussian process regression (GPR) [76] with the Gibbs kernel to reduce fluctuations due to the limited sample size. The  $m_{\gamma\gamma}$  distribution of the continuum background is found to have a smoothly falling shape. The analytic function chosen to model the continuum background is either a power-law function, a Bernstein polynomial [12], or an exponential function of a polynomial, and it is selected for each  $OO$  bin independently. The selected function should have the smallest spurious signal, defined as the systematic bias in the fitted signal yield due to differences between the fit function choice and the background template. The coefficients of these functions are considered to be independent across categories, and in all cases are treated as free parameters in the fits to data. More details can be found in Ref. [12].

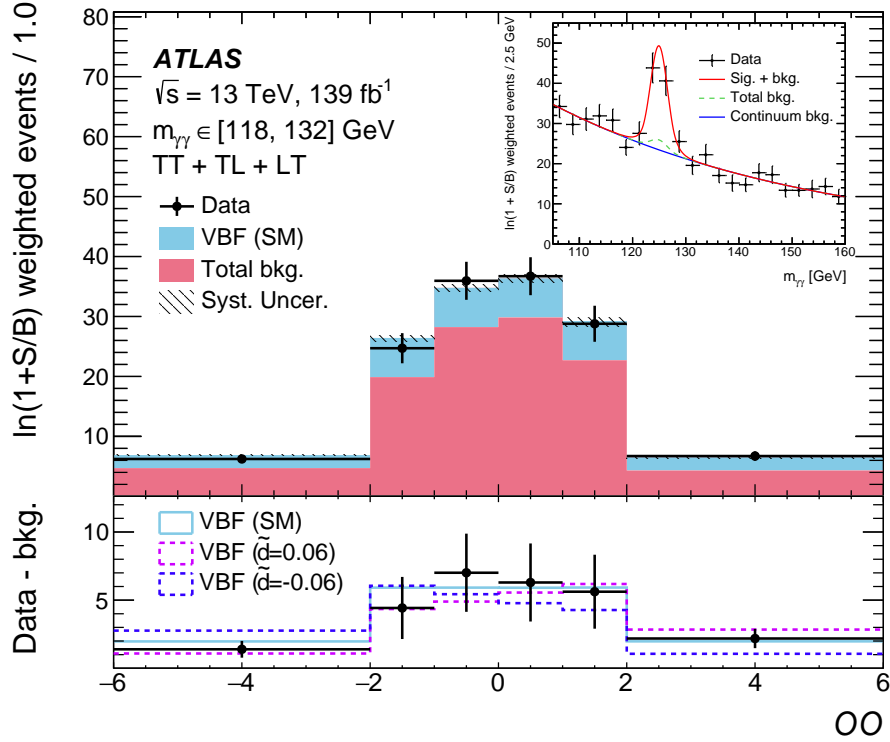


Figure 2: Distribution of the optimal observable  $OO$  for events with  $m_{\gamma\gamma} \in [118, 132] \text{ GeV}$ . Contributions in three signal regions are summed together with a weight of  $\ln(1+S/B)$  for each signal region, where  $S$  and  $B$  are the expected yields of signal and background events with  $m_{\gamma\gamma} \in [118, 132] \text{ GeV}$ . The overflow and underflow are included in the highest and lowest bin, respectively. The uncertainty band shown includes all systematic uncertainties. The weighted summed  $m_{\gamma\gamma}$  distribution of data events is shown in the inner panel along with the signal and background contributions. The lower panel is the  $OO$  distribution in data after subtraction of all backgrounds, in comparison with the SM VBF process, and VBF processes with  $\tilde{d} = 0.06$  and  $\tilde{d} = -0.06$ . The sensitivity to  $\tilde{d}$  is dominated by the tails of the  $OO$  distribution.

An unbinned likelihood is constructed with the  $m_{\gamma\gamma}$  spectra of each  $OO$  bin in signal regions TT, TL and LT. The negative log-likelihood (NLL) is evaluated for various  $\tilde{d}$  and  $c_{H\tilde{W}}$  hypotheses. Confidence intervals are obtained by reading values off the NLL curve, which is constructed by interpolating between the points



with spline functions. The normalization of the signal is allowed to float in the fit. The analysis therefore exploits only the shape of the distribution of the Optimal Observable, and ignores the potential dependence of the inclusive cross-section on CP-mixing scenarios. If present, any BSM CP-even effects would mainly change the normalization, and produce very small symmetric changes in the  $OO$  distribution, which are found to not bias the parameter of interest for the CP-odd effect. All other Higgs boson production modes are considered as backgrounds and are normalized to their SM predicted yields. The expected  $\Delta\text{NLL}$  curve is obtained using a pseudo-dataset where the event yields and distributions in the signal regions are set to the SM expectations for both the signal and background processes.

Both the theoretical and experimental systematic uncertainties are incorporated into the likelihood model of the measurement as nuisance parameters. Theoretical uncertainties arise from the modeling of VBF and ggF processes because of the missing higher-order terms in the perturbative QCD calculations, the modeling of the underlying event and parton shower, the parton distribution functions, and the value of  $\alpha_s$ . These uncertainties are estimated by following the procedure described in Ref. [12]. The experimental uncertainties include the uncertainties in the photon energy scale and resolution [65], the jet energy scale and resolution [77], the luminosity measurement, and the modeling of pileup events and the photon identification and isolation criteria [78]. The spurious signal that could arise from mismodeling of continuum background is estimated in each  $OO$  bin.

Figure 3 shows the  $\Delta\text{NLL}$  curves as functions of  $\tilde{d}$  or  $c_{H\tilde{W}}$ . Here, the  $\tilde{d}$  results use the interference-plus-quadratic terms in Eq. (1), while the  $c_{H\tilde{W}}$  results use only the interference term. The confidence intervals for the two scenarios, interference-only and interference-plus-quadratic, are shown in Table 1. The difference between the results in the two scenarios is found to be small. The results are compatible with the SM and the precision is limited by the statistical uncertainty of the data. For example, the total impact on the 95% confidence intervals of  $\tilde{d}$  from the systematic uncertainty is less than 2%. The measurement is sensitive enough to determine an observed 95% confidence interval for  $\tilde{d}$ , which was not achieved in previous analyses. The expected 68% confidence interval shown for the  $H \rightarrow \tau\tau$  channel in Table 1 differs slightly from that presented in Ref. [9], where the expected  $H \rightarrow \tau\tau$  results were obtained with the nuisance parameters constrained only by the control regions. In the present analysis, the expected results are obtained with the nuisance parameters constrained by both the control regions and signal regions.

The 95% confidence interval for  $c_{H\tilde{W}}$  obtained using the interference-only term is a factor of five more restrictive than in the  $H \rightarrow \gamma\gamma$  differential measurement reported in Ref. [12] because of the dedicated BDTs for the VBF signal selection and the use of the Optimal Observable. The 68% confidence interval for  $c_{H\tilde{W}}$  is about twice as restrictive as that from either the ATLAS or CMS  $H \rightarrow ZZ$  four-lepton analysis [13, 16]. Compared to the previous results for  $H \rightarrow \tau\tau$  [9], based on the interference-plus-quadratic scenario, the expected 68% confidence interval for  $\tilde{d}$  has been tightened by about 20%. After combining the present results with the  $H \rightarrow \tau\tau$  results, the expected confidence intervals are further improved by about 15%. The luminosity uncertainty of the data in 2015–2016, the uncertainties of the electron/photon energy scale and resolution, and the theoretical uncertainty of VBF and ggF processes are correlated in the combination. The jet-related uncertainties are not correlated since a different jet reconstruction technique was used in the  $H \rightarrow \tau\tau$  analysis.

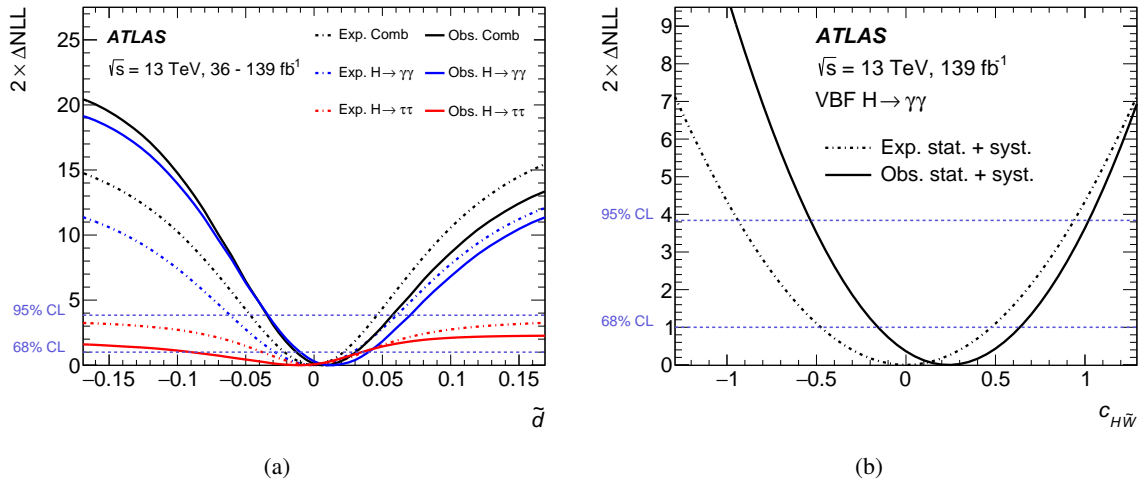


Figure 3:  $\Delta\text{NLL}$  curves as a function of (a)  $\tilde{d}$  and (b)  $c_{H\tilde{W}}$ . In figure (a), the  $\Delta\text{NLL}$  of  $\tilde{d}$  considers the interference-plus-quadratic terms, whereas in figure (b) the  $\Delta\text{NLL}$  of  $c_{H\tilde{W}}$  considers the interference-only term. The solid lines are the observed results, while the dashed lines are the expected results. In figure (a), the blue lines represent the results of this analysis, while the red lines represent the results from the  $H \rightarrow \tau\tau$  analysis [9]. The black lines show the combination of these two analyses. For all figures, the dashed horizontal lines show the values of  $\Delta\text{NLL}$  used to define the 68% and 95% confidence intervals.

Table 1: Observed and expected 68% and 95% confidence intervals for  $\tilde{d}$  and  $c_{H\tilde{W}}$ . Results for scenarios with the interference-only (noted as ‘inter. only’) term and interference-plus-quadratic terms (noted as ‘inter.+quad.’) are both presented. Combined results for  $\tilde{d}$  including the  $H \rightarrow \tau\tau$  analysis [9] are shown. The expected results of  $H \rightarrow \tau\tau$  are slightly different from Ref. [9] due to the different correlation scheme between their signal region and control region.

	68% (exp.)	95% (exp.)	68% (obs.)	95% (obs.)
$\tilde{d}$ (inter. only)	[−0.027, 0.027]	[−0.055, 0.055]	[−0.011, 0.036]	[−0.032, 0.059]
$\tilde{d}$ (inter.+quad.)	[−0.028, 0.028]	[−0.061, 0.060]	[−0.010, 0.040]	[−0.034, 0.071]
$\tilde{d}$ from $H \rightarrow \tau\tau$	[−0.038, 0.036]	–	[−0.090, 0.035]	–
Combined $\tilde{d}$	[−0.022, 0.021]	[−0.046, 0.045]	[−0.012, 0.030]	[−0.034, 0.057]
$c_{H\tilde{W}}$ (inter. only)	[−0.48, 0.48]	[−0.94, 0.94]	[−0.16, 0.64]	[−0.53, 1.02]
$c_{H\tilde{W}}$ (inter.+quad.)	[−0.48, 0.48]	[−0.95, 0.95]	[−0.15, 0.67]	[−0.55, 1.07]

In conclusion, a test of CP invariance in Higgs boson production via vector-boson fusion is performed in the  $H \rightarrow \gamma\gamma$  channel using  $139 \text{ fb}^{-1}$  of  $\sqrt{s} = 13 \text{ TeV}$  proton–proton collision data collected by the ATLAS detector at the LHC. The Optimal Observable method is used to probe CP-violating interactions between the Higgs boson and electroweak gauge bosons described by an effective field theory. The results are compatible with the SM. No sign of CP violation is observed in the Optimal Observable distributions. The constraints on CP-violating effects in the  $HVV$  coupling are the most stringent to date. They allow 68% and 95% confidence intervals to be set for parameters describing the strength of the CP-odd component in the  $HVV$  coupling in two effective field theory bases:  $\tilde{d}$  in the HISZ basis and  $c_{H\tilde{W}}$  in the Warsaw basis. The sensitivity is sufficient to set a 95% confidence interval for  $\tilde{d}$  for the first time, and the constraints on  $\tilde{d}$  are tightened further by combining them with previous results from the  $H \rightarrow \tau\tau$  channel. The constraints



on  $c_{H\tilde{W}}$  are about twice as restrictive as those from either the ATLAS or CMS four-lepton analysis.

## Appendix

*Appendix: BDT based event categorization.* —This analysis uses two BDTs to enrich the VBF signal purity:  $\text{BDT}_{\text{VBF}/\text{ggF}}$  and  $\text{BDT}_{\text{VBF}/\text{Continuum}}$ , which are trained to separate the VBF signal from ggF background and continuum background, respectively. Figure 4 shows the distributions of the BDT output, as well as the requirements for the event categorization. The left panel shows the two-dimensional distributions of  $\text{BDT}_{\text{VBF}/\text{continuum}}$  v.s.  $\text{BDT}_{\text{VBF}/\text{ggF}}$  for both data in the  $m_{\gamma\gamma}$  sideband and VBF signal which are normalized to unity. The vertical line at 0.15 indicates the requirement on  $\text{BDT}_{\text{VBF}/\text{ggF}}$  to separate the tight and loose regions. The ratio of VBF signal over ggF background is improved by a factor of ten in the tight region. The horizontal line at 0.32 (0.09) indicates the requirement on  $\text{BDT}_{\text{VBF}/\text{Continuum}}$  in the  $\text{BDT}_{\text{VBF}/\text{ggF}}$  tight (loose) region, to maximize the combined significance for the VBF signal. The events are finally categorized into four regions: TT, TL, LT, and LL. The right panel shows the  $\text{BDT}_{\text{VBF}/\text{continuum}}$  distributions in the  $\text{BDT}_{\text{VBF}/\text{ggF}}$  tight and loose regions, while the inclusive  $\text{BDT}_{\text{VBF}/\text{ggF}}$  distribution is shown in Figure 1.

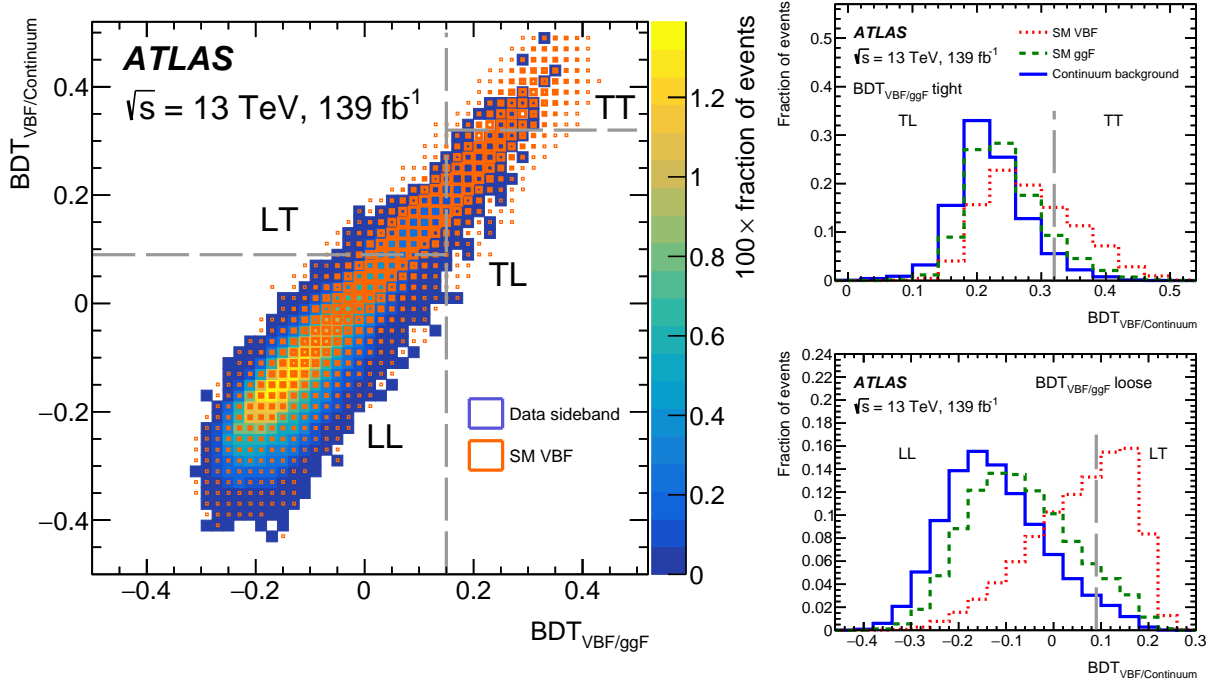


Figure 4: Left: Normalized two-dimensional distributions of  $\text{BDT}_{\text{VBF}/\text{continuum}}$  v.s.  $\text{BDT}_{\text{VBF}/\text{ggF}}$  for both data in the  $m_{\gamma\gamma}$  sideband and VBF signal. The vertical line indicates the requirement on  $\text{BDT}_{\text{VBF}/\text{ggF}}$  to separate the tight and loose regions, while the horizontal lines indicate the requirements on  $\text{BDT}_{\text{VBF}/\text{continuum}}$ . The events are categorized into four regions: TT, TL, LT, and LL. Right:  $\text{BDT}_{\text{VBF}/\text{continuum}}$  distributions in the  $\text{BDT}_{\text{VBF}/\text{ggF}}$  tight and loose regions. The vertical lines indicate the requirements on  $\text{BDT}_{\text{VBF}/\text{continuum}}$ .

## References

- [1] A. D. Sakharov, *Violation of CP Invariance, C asymmetry, and baryon asymmetry of the universe*, *Pisma Zh. Eksp. Teor. Fiz.* **5** (1967) 32.
- [2] M. Kobayashi and T. Maskawa, *CP Violation in the Renormalizable Theory of Weak Interaction*, *Prog. Theor. Phys.* **49** (1973) 652.
- [3] M. B. Gavela, P. Hernandez, J. Orloff, and O. Pene, *Standard model CP violation and baryon asymmetry*, *Mod. Phys. Lett. A* **9** (1994) 795, arXiv: [hep-ph/9312215](#).
- [4] A. G. Cohen, D. B. Kaplan, and A. E. Nelson, *Progress in Electroweak Baryogenesis*, *Ann. Rev. Nucl. Part. Sci.* **43** (1993) 27, arXiv: [hep-ph/9302210](#).
- [5] P. Huet and E. Sather, *Electroweak baryogenesis and standard model CP violation*, *Phys. Rev. D* **51** (1995) 379, arXiv: [hep-ph/9404302](#).
- [6] ATLAS Collaboration, *Observation of a new particle in the search for the Standard Model Higgs boson with the ATLAS detector at the LHC*, *Phys. Lett. B* **716** (2012) 1, arXiv: [1207.7214 \[hep-ex\]](#).
- [7] CMS Collaboration, *Observation of a new boson at a mass of 125 GeV with the CMS experiment at the LHC*, *Phys. Lett. B* **716** (2012) 30, arXiv: [1207.7235 \[hep-ex\]](#).
- [8] L. Evans and P. Bryant, *LHC Machine*, *JINST* **3** (2008) S08001.
- [9] ATLAS Collaboration, *Test of CP invariance in vector-boson fusion production of the Higgs boson in the  $H \rightarrow \tau\tau$  channel in proton-proton collisions at  $\sqrt{s} = 13$  TeV with the ATLAS detector*, *Phys. Lett. B* **805** (2020) 135426, arXiv: [2002.05315 \[hep-ex\]](#).
- [10] ATLAS Collaboration, *CP Properties of Higgs Boson Interactions with Top Quarks in the  $t\bar{t}H$  and  $tH$  Processes Using  $H \rightarrow \gamma\gamma$  with the ATLAS Detector*, *Phys. Rev. Lett.* **125** (2020) 061802, arXiv: [2004.04545 \[hep-ex\]](#).
- [11] ATLAS Collaboration, *Constraints on Higgs boson properties using  $WW^*(\rightarrow e\nu\mu\nu)jj$  production in  $36.1\text{ fb}^{-1}$  of  $\sqrt{s} = 13$  TeV  $pp$  collisions with the ATLAS detector*, (2021), arXiv: [2109.13808 \[hep-ex\]](#).
- [12] ATLAS Collaboration, *Measurements of the Higgs boson inclusive and differential fiducial cross-sections in the diphoton decay channel with  $pp$  collisions at  $\sqrt{s} = 13$  TeV with the ATLAS detector*, (2022), arXiv: [2202.00487 \[hep-ex\]](#).
- [13] ATLAS Collaboration, *Higgs boson production cross-section measurements and their EFT interpretation in the  $4\ell$  decay channel at  $\sqrt{s} = 13$  TeV with the ATLAS detector*, *Eur. Phys. J. C* **80** (2020) 957, [Erratum: *Eur. Phys. J. C* 81 (2021) 29, Erratum: *Eur. Phys. J. C* 81 (2021) 398], arXiv: [2004.03447 \[hep-ex\]](#).
- [14] CMS Collaboration, *Constraints on anomalous  $HVV$  couplings from the production of Higgs bosons decaying to  $\tau$  lepton pairs*, *Phys. Rev. D* **100** (2019) 112002, arXiv: [1903.06973 \[hep-ex\]](#).
- [15] CMS Collaboration, *Measurements of  $t\bar{t}H$  Production and the CP Structure of the Yukawa Interaction between the Higgs Boson and Top Quark in the Diphoton Decay Channel*, *Phys. Rev. Lett.* **125** (2020) 061801, arXiv: [2003.10866 \[hep-ex\]](#).

- [16] CMS Collaboration, *Constraints on anomalous Higgs boson couplings to vector bosons and fermions in its production and decay using the four-lepton final state*, [Phys. Rev. D \*\*104\*\* \(2021\) 052004](#), arXiv: [2104.12152 \[hep-ex\]](#).
- [17] CMS Collaboration, *Analysis of the CP structure of the Yukawa coupling between the Higgs boson and  $\tau$  leptons in proton–proton collisions at  $\sqrt{s} = 13$  TeV*, (2021), arXiv: [2110.04836 \[hep-ex\]](#).
- [18] CMS Collaboration, *Constraints on anomalous Higgs boson couplings to vector bosons and fermions from the production of Higgs bosons using the  $\tau\tau$  final state*, (2022), arXiv: [2205.05120 \[hep-ex\]](#).
- [19] A. Azatov, R. Contino, C. S. Machado, and F. Riva, *Helicity selection rules and noninterference for BSM amplitudes*, [Phys. Rev. D \*\*95\*\* \(2017\) 065014](#), arXiv: [1607.05236 \[hep-ph\]](#).
- [20] ALEPH Collaboration, *Improved measurement of the triple gauge-boson couplings  $\gamma WW$  and  $ZWW$  in  $e^+e^-$  collisions*, [Phys. Lett. B \*\*614\*\* \(2005\) 7](#).
- [21] OPAL Collaboration, *Measurement of W boson polarizations and CP violating triple gauge couplings from  $W^+W^-$  production at LEP*, [Eur. Phys. J. C \*\*19\*\* \(2001\) 229](#), arXiv: [hep-ex/0009021](#).
- [22] M. Davier, L. Duflot, F. Le Diberder, and A. Rouge, *The Optimal method for the measurement of tau polarization*, [Phys. Lett. B \*\*306\*\* \(1993\) 411](#).
- [23] D. Atwood and A. Soni, *Analysis for magnetic moment and electric dipole moment form factors of the top quark via  $e^+e^- \rightarrow tt^-$* , [Phys. Rev. D \*\*45\*\* \(7 1992\) 2405](#), URL: <https://link.aps.org/doi/10.1103/PhysRevD.45.2405>.
- [24] M. Diehl and O. Nachtmann, *Optimal observables for the measurement of three gauge boson couplings in  $e^+e^- \rightarrow W^+W^-$* , [Z. Phys. C \*\*62\*\* \(1994\) 397](#).
- [25] J. Brehmer, F. Kling, T. Plehn, and T. M. P. Tait, *Better Higgs-CP tests through information geometry*, [Phys. Rev. D \*\*97\*\* \(2018\) 095017](#), arXiv: [1712.02350 \[hep-ph\]](#).
- [26] K. Hagiwara, S. Ishihara, R. Szalapski, and D. Zeppenfeld, *Low energy effects of new interactions in the electroweak boson sector*, [Phys. Rev. D \*\*48\*\* \(1993\) 2182](#).
- [27] I. Brivio, Y. Jiang, and M. Trott, *The SMEFTsim package, theory and tools*, [JHEP \*\*12\*\* \(2017\) 070](#), arXiv: [1709.06492 \[hep-ph\]](#).
- [28] I. Brivio, *SMEFTsim 3.0 — a practical guide*, [JHEP \*\*04\*\* \(2021\) 073](#), arXiv: [2012.11343 \[hep-ph\]](#).
- [29] B. Grzadkowski, M. Iskrzynski, M. Misiak, and J. Rosiek, *Dimension-six terms in the Standard Model Lagrangian*, [JHEP \*\*10\*\* \(2010\) 085](#), arXiv: [1008.4884 \[hep-ph\]](#).
- [30] ATLAS Collaboration, *The ATLAS Experiment at the CERN Large Hadron Collider*, [JINST \*\*3\*\* \(2008\) S08003](#).
- [31] B. Abbott et al., *Production and integration of the ATLAS Insertable B-Layer*, [JINST \*\*13\*\* \(2018\) T05008](#), arXiv: [1803.00844 \[physics.ins-det\]](#).

- [32] ATLAS Collaboration, *ATLAS Insertable B-Layer: Technical Design Report*, ATLAS-TDR-19; CERN-LHCC-2010-013, 2010, URL: <https://cds.cern.ch/record/1291633>, Addendum: ATLAS-TDR-19-ADD-1; CERN-LHCC-2012-009, 2012, URL: <https://cds.cern.ch/record/1451888>.
- [33] ATLAS Collaboration, *Performance of the ATLAS trigger system in 2015*, *Eur. Phys. J. C* **77** (2017) 317, arXiv: [1611.09661](https://arxiv.org/abs/1611.09661) [hep-ex].
- [34] ATLAS Collaboration, *Performance of electron and photon triggers in ATLAS during LHC Run 2*, *Eur. Phys. J. C* **80** (2020) 47, arXiv: [1909.00761](https://arxiv.org/abs/1909.00761) [hep-ex].
- [35] ATLAS Collaboration, *The ATLAS Collaboration Software and Firmware*, ATL-SOFT-PUB-2021-001, 2021, URL: <https://cds.cern.ch/record/2767187>.
- [36] P. Nason and C. Oleari, *NLO Higgs boson production via vector-boson fusion matched with shower in POWHEG*, *JHEP* **02** (2010) 037, arXiv: [0911.5299](https://arxiv.org/abs/0911.5299) [hep-ph].
- [37] J. Butterworth et al., *PDF4LHC recommendations for LHC Run II*, *J. Phys. G* **43** (2016) 023001, arXiv: [1510.03865](https://arxiv.org/abs/1510.03865) [hep-ph].
- [38] M. Ciccolini, A. Denner, and S. Dittmaier, *Strong and Electroweak Corrections to the Production of a Higgs Boson + 2 Jets via Weak Interactions at the Large Hadron Collider*, *Phys. Rev. Lett.* **99** (2007) 161803, arXiv: [0707.0381](https://arxiv.org/abs/0707.0381) [hep-ph].
- [39] M. Ciccolini, A. Denner, and S. Dittmaier, *Electroweak and QCD corrections to Higgs production via vector-boson fusion at the CERN LHC*, *Phys. Rev. D* **77** (2008) 013002, arXiv: [0710.4749](https://arxiv.org/abs/0710.4749) [hep-ph].
- [40] P. Bolzoni, F. Maltoni, S.-O. Moch, and M. Zaro, *Higgs Boson Production via Vector-Boson Fusion at Next-to-Next-to-Leading Order in QCD*, *Phys. Rev. Lett.* **105** (2010) 011801, arXiv: [1003.4451](https://arxiv.org/abs/1003.4451) [hep-ph].
- [41] K. Hamilton, P. Nason, E. Re, and G. Zanderighi, *NNLOPS simulation of Higgs boson production*, *JHEP* **10** (2013) 222, arXiv: [1309.0017](https://arxiv.org/abs/1309.0017) [hep-ph].
- [42] K. Hamilton, P. Nason, and G. Zanderighi, *Finite quark-mass effects in the NNLOPS POWHEG+MiNLO Higgs generator*, *JHEP* **05** (2015) 140, arXiv: [1501.04637](https://arxiv.org/abs/1501.04637) [hep-ph].
- [43] K. Hamilton, P. Nason, and G. Zanderighi, *MINLO: multi-scale improved NLO*, *JHEP* **10** (2012) 155, arXiv: [1206.3572](https://arxiv.org/abs/1206.3572) [hep-ph].
- [44] J. M. Campbell et al., *NLO Higgs boson production plus one and two jets using the POWHEG BOX, MadGraph4 and MCFM*, *JHEP* **07** (2012) 092, arXiv: [1202.5475](https://arxiv.org/abs/1202.5475) [hep-ph].
- [45] K. Hamilton, P. Nason, C. Oleari, and G. Zanderighi, *Merging H/W/Z + 0 and 1 jet at NLO with no merging scale: a path to parton shower + NNLO matching*, *JHEP* **05** (2013) 082, arXiv: [1212.4504](https://arxiv.org/abs/1212.4504) [hep-ph].
- [46] S. Catani and M. Grazzini, *Next-to-Next-to-Leading-Order Subtraction Formalism in Hadron Collisions and its Application to Higgs-boson Production at the Large Hadron Collider*, *Phys. Rev. Lett.* **98** (2007) 222002, arXiv: [hep-ph/0703012](https://arxiv.org/abs/hep-ph/0703012) [hep-ph].
- [47] D. de Florian et al., *Handbook of LHC Higgs Cross Sections: 4. Deciphering the Nature of the Higgs Sector*, (2016), arXiv: [1610.07922](https://arxiv.org/abs/1610.07922) [hep-ph].

- [48] C. Anastasiou et al., *High precision determination of the gluon fusion Higgs boson cross-section at the LHC*, *JHEP* **05** (2016) 058, arXiv: [1602.00695 \[hep-ph\]](#).
- [49] C. Anastasiou, C. Duhr, F. Dulat, F. Herzog, and B. Mistlberger, *Higgs Boson Gluon-Fusion Production in QCD at Three Loops*, *Phys. Rev. Lett.* **114** (2015) 212001, arXiv: [1503.06056 \[hep-ph\]](#).
- [50] F. Dulat, A. Lazopoulos, and B. Mistlberger, *iHixs 2 – Inclusive Higgs cross sections*, *Comput. Phys. Commun.* **233** (2018) 243, arXiv: [1802.00827 \[hep-ph\]](#).
- [51] R. V. Harlander and K. J. Ozeren, *Finite top mass effects for hadronic Higgs production at next-to-next-to-leading order*, *JHEP* **11** (2009) 088, arXiv: [0909.3420 \[hep-ph\]](#).
- [52] R. V. Harlander and K. J. Ozeren, *Top mass effects in Higgs production at next-to-next-to-leading order QCD: Virtual corrections*, *Phys. Lett. B* **679** (2009) 467, arXiv: [0907.2997 \[hep-ph\]](#).
- [53] R. V. Harlander, H. Mantler, S. Marzani, and K. J. Ozeren, *Higgs production in gluon fusion at next-to-next-to-leading order QCD for finite top mass*, *Eur. Phys. J. C* **66** (2010) 359, arXiv: [0912.2104 \[hep-ph\]](#).
- [54] A. Pak, M. Rogal, and M. Steinhauser, *Finite top quark mass effects in NNLO Higgs boson production at LHC*, *JHEP* **02** (2010) 025, arXiv: [0911.4662 \[hep-ph\]](#).
- [55] S. Actis, G. Passarino, C. Sturm, and S. Uccirati, *NLO electroweak corrections to Higgs boson production at hadron colliders*, *Phys. Lett. B* **670** (2008) 12, arXiv: [0809.1301 \[hep-ph\]](#).
- [56] S. Actis, G. Passarino, C. Sturm, and S. Uccirati, *NNLO computational techniques: The cases  $H \rightarrow \gamma\gamma$  and  $H \rightarrow gg$* , *Nucl. Phys. B* **811** (2009) 182, arXiv: [0809.3667 \[hep-ph\]](#).
- [57] M. Bonetti, K. Melnikov, and L. Tancredi, *Higher order corrections to mixed QCD-EW contributions to Higgs boson production in gluon fusion*, *Phys. Rev. D* **97** (2018) 056017, arXiv: [1801.10403 \[hep-ph\]](#), Erratum: *Phys. Rev. D* **97** (2018) 099906.
- [58] E. Bothmann et al., *Event Generation with Sherpa 2.2*, *SciPost Phys.* **7** (2019) 034, arXiv: [1905.09127 \[hep-ph\]](#).
- [59] A. Denner, S. Dittmaier, S. Kallweit, and A. Mück, *HAWK 2.0: A Monte Carlo program for Higgs production in vector-boson fusion and Higgs strahlung at hadron colliders*, *Comput. Phys. Commun.* **195** (2015) 161, arXiv: [1412.5390 \[hep-ph\]](#).
- [60] J. Alwall et al., *The automated computation of tree-level and next-to-leading order differential cross sections, and their matching to parton shower simulations*, *JHEP* **07** (2014) 079, arXiv: [1405.0301 \[hep-ph\]](#).
- [61] R. Frederix and S. Frixione, *Merging meets matching in MC@NLO*, *JHEP* **12** (2012) 061, arXiv: [1209.6215 \[hep-ph\]](#).
- [62] ATLAS Collaboration, *The ATLAS Simulation Infrastructure*, *Eur. Phys. J. C* **70** (2010) 823, arXiv: [1005.4568 \[physics.ins-det\]](#).
- [63] GEANT4 Collaboration, *GEANT4—a simulation toolkit*, *Nucl. Instrum. Meth. A* **506** (2003) 250.



- [64] T. Sjöstrand et al., *An introduction to PYTHIA 8.2*, *Comput. Phys. Commun.* **191** (2015) 159, arXiv: [1410.3012 \[hep-ph\]](#).
- [65] ATLAS Collaboration, *Electron and photon performance measurements with the ATLAS detector using the 2015–2017 LHC proton–proton collision data*, *JINST* **14** (2019) P12006, arXiv: [1908.00005 \[hep-ex\]](#).
- [66] ATLAS Collaboration, *Measurement of Higgs boson production in the diphoton decay channel in  $pp$  collisions at center-of-mass energies of 7 and 8 TeV with the ATLAS detector*, *Phys. Rev. D* **90** (2014) 112015, arXiv: [1408.7084 \[hep-ex\]](#).
- [67] M. Cacciari, G. P. Salam, and G. Soyez, *The anti- $k_t$  jet clustering algorithm*, *JHEP* **04** (2008) 063, arXiv: [0802.1189 \[hep-ph\]](#).
- [68] M. Cacciari, G. P. Salam, and G. Soyez, *FastJet user manual*, *Eur. Phys. J. C* **72** (2012) 1896, arXiv: [1111.6097 \[hep-ph\]](#).
- [69] ATLAS Collaboration, *Optimisation of large-radius jet reconstruction for the ATLAS detector in 13 TeV proton–proton collisions*, *Eur. Phys. J. C* **81** (2020) 334, arXiv: [2009.04986 \[hep-ex\]](#).
- [70] ATLAS Collaboration, *Performance of pile-up mitigation techniques for jets in  $pp$  collisions at  $\sqrt{s} = 8$  TeV using the ATLAS detector*, *Eur. Phys. J. C* **76** (2016) 581, arXiv: [1510.03823 \[hep-ex\]](#).
- [71] ATLAS Collaboration, *Identification and rejection of pile-up jets at high pseudorapidity with the ATLAS detector*, *Eur. Phys. J. C* **77** (2017) 580, arXiv: [1705.02211 \[hep-ex\]](#),  
Erratum: *Eur. Phys. J. C* **77** (2017) 712.
- [72] J. R. Andersen, K. Arnold, and D. Zeppenfeld, *Azimuthal angle correlations for Higgs boson plus multi-jet events*, *JHEP* **06** (2010) 091, arXiv: [1001.3822 \[hep-ph\]](#).
- [73] A. Hoecker et al., *TMVA - Toolkit for Multivariate Data Analysis*, 2007, arXiv: [physics/0703039 \[physics.data-an\]](#).
- [74] ATLAS Collaboration, *Measurements of Higgs boson production and couplings in diboson final states with the ATLAS detector at the LHC*, *Phys. Lett. B* **726** (2013) 88, arXiv: [1307.1427 \[hep-ex\]](#), Erratum: *Phys. Lett. B* **734** (2014) 406.
- [75] ATLAS Collaboration, *Measurement of the isolated diphoton cross section in  $pp$  collisions at  $\sqrt{s} = 7$  TeV with the ATLAS detector*, *Phys. Rev. D* **85** (2012) 012003, arXiv: [1107.0581 \[hep-ex\]](#).
- [76] M. Frate, K. Cranmer, S. Kalia, A. Vandenberg-Rodes, and D. Whiteson, *Modeling Smooth Backgrounds and Generic Localized Signals with Gaussian Processes*, (2017), arXiv: [1709.05681 \[physics.data-an\]](#).
- [77] ATLAS Collaboration, *Jet energy scale and resolution measured in proton–proton collisions at  $\sqrt{s} = 13$  TeV with the ATLAS detector*, *Eur. Phys. J. C* **81** (2020) 689, arXiv: [2007.02645 \[hep-ex\]](#).
- [78] ATLAS Collaboration, *Measurement of the photon identification efficiencies with the ATLAS detector using LHC Run 2 data collected in 2015 and 2016*, *Eur. Phys. J. C* **79** (2019) 205, arXiv: [1810.05087 \[hep-ex\]](#).